

Phase Behavior in the Active Layer of Small Molecule Organic
Photovoltaics: State Diagram of p-DTS(FBTTh2)(2):PC71BM

Peer-reviewed author version

Van den Brande, Niko; Defour, Maxime; DEVISSCHER, Dries; VERSTAPPEN, Pieter; REEKMANS, Gunter; D'HAEN, Jan; ADRIAENSENS, Peter; MAES, Wouter; Van Assche, Guy & Van Mele, Bruno (2020) Phase Behavior in the Active Layer of Small Molecule Organic Photovoltaics: State Diagram of p-DTS(FBTTh2)(2):PC71BM. In: JOURNAL OF PHYSICAL CHEMISTRY C, 124 (13) , p. 7566 -7577.

DOI: 10.1021/acs.jpcc.0c00808

Handle: <http://hdl.handle.net/1942/31178>

The Phase Behavior in the Active Layer of Small Molecule Organic Photovoltaics: the State Diagram of p-DTS(FBTTh₂)₂:PC₇₁BM

Niko Van den Brande^{1*}, Maxime Defour¹, Dries Devisscher^{2,3}, Pieter Verstappen^{2,3}, Gunter Reekmans⁴, Jan D'Haen⁵, Peter Adriaenssens^{3,4}, Wouter Maes^{2,3}, Guy Van Assche¹, Bruno Van Mele¹

¹ Physical Chemistry and Polymer Science (FYSC), Vrije Universiteit Brussel (VUB), Pleinlaan 2, 1050 Brussels, Belgium

² Design & Synthesis of Organic Semiconductors (DSOS), Institute for Materials Research (IMO-IMOMEC), Hasselt University, Universitaire Campus, 3590 Diepenbeek, Belgium

³ imec, Associated Laboratory IMOMEC, Wetenschapspark 1, 3590 Diepenbeek, Belgium

⁴ Applied and Analytical Chemistry, Institute for Materials Research (IMO-IMOMEC), Hasselt University, Universitaire Campus, Agoralaan 1, 3590 Diepenbeek, Belgium

⁵ Electrical and Physical Characterisation (ELPHYC), Institute for Materials Research (IMO-IMOMEC), Hasselt University, Wetenschapspark 1, Agoralaan 1, 3590 Diepenbeek, Belgium

*Corresponding author

E-mail: npvdbran@vub.be

Abstract

A comprehensive study was undertaken to obtain a more fundamental understanding of the phase behavior of the p-DTS(FBTTh₂)₂:PC₇₁BM system, used in small molecule organic solar cells, with a strong focus on the amorphous phase and its influence on crystallinity. Three dedicated thermal protocols were used in combination with advanced thermal analysis, solid-state NMR, and wide angle X-ray diffraction. Rapid cooling, to avoid structure formation and gain insight in the amorphous phase, and slow cooling, to promote structure formation, were used as limiting cases to explain the intermediate behavior after device processing from solution. A complete state diagram was developed and the glass transition (T_g) - composition relationship was determined. In the case of slow cooling and the procedure used for device processing, the rapid crystallization of p-DTS(FBTTh₂)₂ leads to an enrichment of the amorphous phase in PC₇₁BM, increasing its T_g and causing vitrification of the mixed amorphous phase before crystallization when the total amount of PC₇₁BM exceeds

70 wt%. The common processing additive 1,8-diiodooctane (DIO) was found to lead to a lower p-DTS(FBTTh₂)₂ crystallinity and smaller average crystal size. More importantly, it acts as a strong plasticizer, lowering T_g significantly and thus reducing the morphological stability of the p-DTS(FBTTh₂)₂:PC₇₁BM mixtures.

1. Introduction

Organic photovoltaics (OPVs) have matured strongly as a research field, becoming a complementary or even alternative technology for classical inorganic solar cells. Because OPV cells are based on thin organic active layers, they exhibit attractive properties such as solvent processability, low weight, and flexibility.^{1,2} By combining an electron donor and an electron acceptor in the photoactive layer, a heterojunction is created that is necessary for excitonic charge generation. The interface between donor and acceptor, where charge separation can take place, should be maximized. A common solution for this is the bulk heterojunction, which is formed by a complex phase separation process during the drying of a solution containing both donor and acceptor.³

Although most of the best performing electron donor materials applied in OPV devices are push-pull type conjugated copolymers⁴⁻⁶ that reduce the band gap and increase photon absorption, significant research interest has also gone into the development of so-called ‘small molecule’ donors.⁷ The highest reported power conversion efficiency (PCE) for organic solar cells based on small molecule donor materials has reached up to 11.7%.⁷⁻¹¹ Despite certain drawbacks compared to polymer materials, e.g. a more narrow absorption and more challenging ink formulation, small molecules also exhibit some appealing advantages, such as their well-defined structure, reduced batch-to-batch variations and more thorough purification options. In this way, structural defects such as homocoupling can be avoided in the final product.¹²⁻¹⁴

Among the high performance small molecule donors, 7,7'-(4,4-bis(2-ethylhexyl)-4*H*-silolo[3,2-*b*:4,5-*b'*]dithiophene-2,6-diyl)bis(6-fluoro-4-(5'-hexyl-[2,2'-bithiophen]-5-yl)benzo[*c*][1,2,5]thiadiazole) (p-DTS(FBTTh₂)₂) has received much research interest since its first synthesis by Bazan and coworkers in 2012.¹⁵ The solar cell efficiency can reach 7.0% in single junction devices with PC₇₁BM as the acceptor by the use of 1,8-diiodooctane (DIO) as a processing additive in combination with thermal annealing.^{15,16} The addition of 0.4% in volume of DIO in chlorobenzene significantly increases the crystallinity of the mixture (important for charge transport) while limiting the crystal size (important for charge

separation by enhancing the donor-acceptor interface).^{15–20} More specifically, the size of the nano-crystals of the donor material in the presence of DIO was roughly six times smaller (ca. 24 nm) than in the film prepared without the processing additive (ca. 134 nm after thermal annealing at 100 °C of as-cast films).²⁰ The effect of DIO on film structure formation seems to be most pronounced during the first 120 seconds of evaporation by favoring and accelerating the rate at which crystals are formed.¹⁸ Since DIO affects mainly the film morphology within the first two minutes of film formation, it was speculated that the additive might form a stable complex with p-DTS(FBTTh₂)₂.¹⁸

The PCE of p-DTS(FBTTh₂)₂:PC₇₁BM solar cells was further increased up to 8.9% by introduction of a ZnO interlayer to increase the charge collection efficiency.²¹ In case p-DTS(FBTTh₂)₂ was combined with a perylenediimide non-fullerene acceptor, PCE values up to 5.1% were achieved.²²

The highly crystalline nature of p-DTS(FBTTh₂)₂ has led to several X-ray studies to analyze mixtures' morphology and understand the mechanism of crystal formation,^{16–20,23–26} and liquid crystallinity.²⁷ p-DTS(FBTTh₂)₂ has recently also been the subject of a study regarding the influence of homocoupling defects on photovoltaic performance and eutectic behaviour.^{28,29}

While the crystalline p-DTS(FBTTh₂)₂ phase is well studied, information on the amorphous phase and its influence on crystallinity is lacking, and therefore also a systematic understanding of the phase behavior of p-DTS(FBTTh₂)₂:PC₇₁BM mixtures of different composition. The determination of the glass transition temperature (T_g) of the active layer is important with respect to device stability. Above T_g , the disordered phase gains mobility and can potentially reorganize towards a more thermodynamically stable morphology. Reorganization of the active layer can be detrimental for device efficiency if it leads to a coarsened morphology with ordered domains that are too large for efficient charge separation. Practically, T_g should be higher than 85 °C to ensure a stable morphology under all working conditions.^{30–32}

Moreover, it was shown that thermal annealing of p-DTS(FBTTh₂)₂:PC₇₁BM active layers may lead to more efficient devices.^{16,20} The choice of the annealing parameters (i.e. temperature and time) is usually based on trial and error after the choice regarding mixture composition.^{16,20} Appropriate annealing parameters to promote reorganization, however, depend on many aspects such as the morphology after solution processing (the initial

morphology of the as-cast mixture), the presence of processing additives, and the T_g and melting temperature (T_m) of the mixture, as the annealing temperature should lie between T_g and T_m . It is important to note that the results mentioned above are based on mixtures prepared using different deposition techniques or processing conditions, which makes it difficult to draw general conclusions regarding the benefits of additives and/or thermal annealing on device efficiency.

In this work, Rapid Heat-Cool differential scanning calorimetry (RHC) is used to investigate the phase behavior of p-DTS(FBTTh₂)₂:PC₇₁BM in a systematic way and the influence of the casting technique and the donor:acceptor ratio on amorphous and crystalline phases. RHC has been established in earlier work as a well-suited thermal analysis technique for the characterization of pure organic electronic materials,^{33,34} for the development of state diagrams of mixtures,^{29,35} and to study the important role of the amorphous phase in the active layer.³⁶ An extra advantage is the monodisperse and low molar mass of p-DTS(FBTTh₂)₂, leading to sharp thermal transitions. The evolution of T_g with the mixture's composition is defined to understand the influence of the amorphous phase on crystallization. As-cast p-DTS(FBTTh₂)₂:PC₇₁BM mixtures, but also slowly and rapidly cooled mixtures from the melt are investigated. Finally, the influence of DIO on thermal transitions is studied. RHC is combined with X-ray diffraction and solid-state NMR relaxometry, which was recently shown to give detailed insights on the nanoscale organization of OPV mixtures,^{37–40} to gain a more complete understanding on the temperature – composition – morphology relationships of these mixtures.

2. Materials and techniques

2.1. Rapid heat-cool differential scanning calorimetry

Thermal analysis was performed using a rapid heat-cool differential scanning calorimeter (RHC), a prototype developed by TA Instruments.^{41,42} Calibration of temperature and enthalpy was performed at a scanning rate of 500 K min⁻¹ using indium and adamantane standards. Experiments were performed using helium (10 mL.min⁻¹) as a purge gas. Dedicated aluminium RHC crucibles were filled with sample masses in the range of 200–250 µg.

2.2. Wide angle X-ray scattering

WAXS measurements were performed with a Bruker D8 diffractometer. This theta-theta diffractometer is equipped with a Göbel mirror (line focus, mostly Cu K α radiation). The X-rays are detected with a 1D lynxeye detector. The measurements were carried out at ambient temperature with θ / 2θ locked coupled scans, from $2\theta = 2^\circ - 30^\circ$ with a step size of $2\theta = 0.01^\circ$ and a collecting time of 2 seconds.

2.3. Solid-state NMR

Solid-state ^1H -wideline NMR (ss-NMR) measurements were carried out at ambient temperature on a Varian Inova 400 spectrometer in a dedicated wide-line probe equipped with a 5 mm coil using the solid echo method. The samples were placed in 5 mm glass tubes, which were closed tightly with Teflon stoppers.

The $T_{1\text{H}}$ relaxation decay times (spin-lattice relaxation in the lab frame) were measured by placing an inversion recovery filter in front of the solid echo part (180°_{x} - t - 90°_{x} - t_{se} - 90°_{y} - t_{se} - acquire). The integrated proton signal intensity was analysed bi- or tri-exponentially as a function of the variable inversion time t according to:

$$I(t) = I_0^{\text{S}}.(1 - 2.\exp(-t/T_{1\text{H}}^{\text{S}})) + I_0^{\text{I}}.(1 - 2.\exp(-t/T_{1\text{H}}^{\text{I}})) + I_0^{\text{L}}.(1 - 2.\exp(-t/T_{1\text{H}}^{\text{L}})) + c^{\text{te}}$$

‘S’, ‘I’ and ‘L’ refer to the fractions with short, intermediate and long decay time, respectively.

The $T_{1\rho\text{H}}$ decay times (spin-lattice relaxation in the rotating frame) were measured by applying a spin-lock field (45 kHz) of variable duration, t_{SL} , after the initial 90°_{x} pulse in the solid echo pulse sequence (90°_{x} - t_{SL} - t_{se} - 90°_{y} - t_{se} - acquire). The integrated proton signal intensity was analysed bi-exponentially as a function of the variable duration of the spin-lock field t_{SL} according to the equation:

$$I(t) = I_0^{\text{S}}.\exp(-t/T_{1\rho\text{H}}^{\text{S}}) + I_0^{\text{L}}.\exp(-t/T_{1\rho\text{H}}^{\text{L}}) + c^{\text{te}}$$

‘S’ and ‘L’ refer to the fractions with short and long decay time, respectively.

All experimental data were analyzed using a non-linear least-squares fit (Levenberg-Marquardt algorithm). A preparation delay of 5 times the longest $T_{1\text{H}}$ relaxation decay time was always respected between successive accumulations to obtain quantitative results. More information regarding the ss-NMR procedure can be found in reference 40.

2.4. Preparation of p-DTS(FBTTh₂)₂:PC₇₁BM mixtures

p-DTS(FBTTh₂)₂, obtained from 1-Material, and PC₇₁BM (purity 99%), purchased from Solenne BV, were used without purification. All samples for RHC, XRD and ss-NMR analysis were prepared following a systematic approach to mimic the device processing conditions as closely as possible.¹⁵ First, 50 mg of different weight compositions of p-DTS(FBTTh₂)₂:PC₇₁BM was dissolved in chlorobenzene at a concentration of 35 mg/mL. The mixtures were prepared without the DIO additive; the effect of DIO was studied separately (see 3.7.). These solutions were then stirred in a sealed vial overnight at 60 °C. After a final stirring step of 15 minutes at 90 °C, the samples were drop casted on a glass substrate at a constant temperature of 90 °C. After a drying time of 2 minutes, the substrate was removed from the heating source and cooled to ambient temperature. The blends were then removed mechanically from the substrate using a razor blade. The acquired solid was subsequently dried under vacuum overnight to remove any residual solvent. The samples were subsequently divided in three sets to investigate the effect of processing. All sets were analyzed by RHC, XRD and ss-NMR. One set was analyzed *as-cast* to simulate the active layer of an OPV device without any specific thermal treatment. Two sets were subjected to additional thermal post-treatments. After an initial melting stage at 320 °C for 10 seconds, one set was quench-cooled by submergence in liquid nitrogen (ballistic cooling) for XRD and ss-NMR samples or by rapid cooling at 500 K.min⁻¹ for RHC samples. This rapid cooling step promotes amorphousness by hindering the development of structural order. The final set was subjected to slow cooling (1 K.min⁻¹) from the melt to promote structural ordering toward thermodynamic equilibrium and the formation of crystallinity. Conventional differential scanning calorimetry (DSC) was used to perform the slow cooling from the melt for the different mixtures measured by XRD and ss-NMR. The powdery mixtures were placed in open crucibles, which were heated to 320 °C in the DSC furnace. The mixtures were then subjected to a relatively fast cooling (50 K.min⁻¹) up to 250 °C to minimize potential degradation. Finally, a slow cooling of 1 K.min⁻¹ was applied.

All RHC thermograms were obtained by rapid heating at 500 K.min⁻¹. The use of high heating rates helps to preserve the effects of preceding processing conditions and reduce or prevent reorganization upon heating (cold crystallization) *and* has a positive effect on the sensitivity by increasing the signal-to-noise ratio of the measurement.

3. Results and discussion

3.1. Thermal characterization of pure p-DTS(FBTTh₂)₂ and PC₇₁BM

Before studying mixtures of p-DTS(FBTTh₂)₂:PC₇₁BM, the thermal behavior of the pure components was first established. The p-DTS(FBTTh₂)₂ donor has been studied thoroughly with RHC in a recent study, where it was found to be highly crystalline.²⁹ Furthermore, it was found to exhibit fast crystallization kinetics. Even when liquid nitrogen was used to cool the material ballistically, an accurate determination of its T_g was impossible due to the rapid onset of cold crystallization. For this reason, the T_g was estimated to be between 35 and 50 °C.²⁹ A more accurate value may be obtained by using fast scanning chip calorimetry,^{43–46} but this was outside the scope of this study. In the current study heating rates of 500 K.min⁻¹ have been used to suppress reorganization as much as possible, yielding a melting enthalpy (ΔH_m) of 45 J.g⁻¹ with an onset and endset of melting of 175 °C and 229 °C, respectively, and a melting temperature (T_m) based on the peak maximum of 208 °C (see Figure 1, (top)).

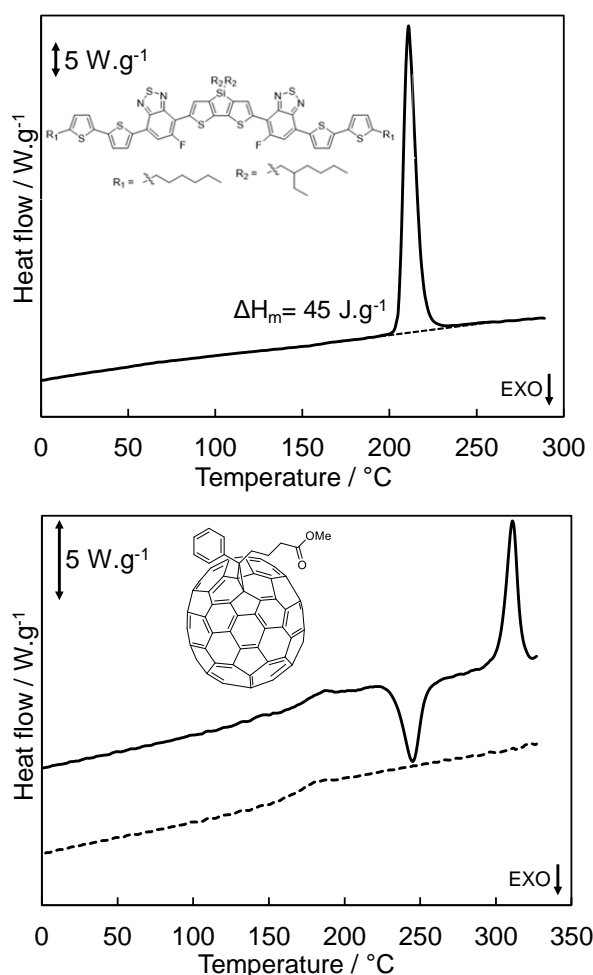


Figure 1: (top) RHC heating curve of p-DTS(FBTTh₂)₂ after slow cooling (1 K.min⁻¹) from the melt. (bottom) RHC heating curves of PC₇₁BM. After undergoing cold crystallization and melting during the first heating (solid line), the material remains amorphous in following heatings (dotted line), after being cooled at 500 K.min⁻¹. The curves are shifted vertically for clarity.

As can be seen in Figure 1 (bottom), the PC₇₁BM acceptor material is found to exhibit a T_g around 172 °C in the first heating, followed by cold crystallization at 245 °C and a melting transition with a peak maximum of 311 °C. Once the crystallization and melting peaks are integrated with a linear baseline, almost identical enthalpies (about 11 J.g⁻¹) are obtained, which means that prior to the first heating the sample was amorphous. During the following heating and cooling cycles at 500 K.min⁻¹ only a T_g of 172 °C is observed, without any crystallization and melting, which again indicates the amorphous nature of the material in these conditions. This T_g value is significantly higher than the 139 °C observed for PC₆₁BM at identical scanning conditions.³⁶

Having determined the thermal behavior of the pure compounds by RHC, their mixtures will be studied after rapid and slow cooling from the melt and in as-cast conditions.

3.2. Characterization of the mixed amorphous phase by rapidly cooling p-DTS(FBTTh₂)₂:PC₇₁BM mixtures

The RHC heating curves of rapidly cooled samples are displayed in Figure 2. Mixtures with less than 60 wt% PC₇₁BM order during the rapid heating, indicating that crystal nucleation occurred during the preceding rapid cooling. However, in all cases except for the 10 wt% PC₇₁BM, the endothermic melting enthalpy is compensated by the exothermic cold crystallization enthalpy, indicating that the mixtures were fully amorphous after rapid cooling. This is not the case for the 10 wt% PC₇₁BM mixture, which also displays a crystallization peak around 110 °C in the preceding fast cooling at 500 K.min⁻¹ (not shown). Note that the cold crystallization peak shifts to higher temperatures with increasing PC₇₁BM content, indicating that the presence of the fullerene derivative hinders the formation of order in the mixture. Cold crystallization is completely inhibited in the samples containing 60 wt% PC₇₁BM or more.

XRD measurements of some of the quench-cooled samples (Figure 3) confirm the amorphous nature by the absence of sharp diffraction peaks. The weak and broad peaks visible at 2 θ \approx 3.9°, 2 θ \approx 16–22° and 2 θ \approx 25–26° could arise either from a partially anisotropic disordered

phase or from the reflection of imperfect crystals with a poor long-range order. This indicates that it is crucial to consider an ‘order/disorder scale’ since the amorphous phase is not necessarily fully disordered, as is often assumed.

It can be concluded that for all mixtures, except 10 wt% PC₇₁BM, the rapid cooling was successful in avoiding any crystallization. The composition of the amorphous phase of the rapidly cooled samples is therefore the same as that of the as-prepared mixtures, so that the measured T_g values can be directly linked to the initial mixture compositions. The unique T_g observed for each mixture corresponds with the presence of one mixed amorphous phase. T_g increases continuously from pure p-DTS(FBTTh₂)₂ (T_g = 35-50 °C) to pure PC₇₁BM (T_g = 172 °C) (see Figure 1 and Figure 4).

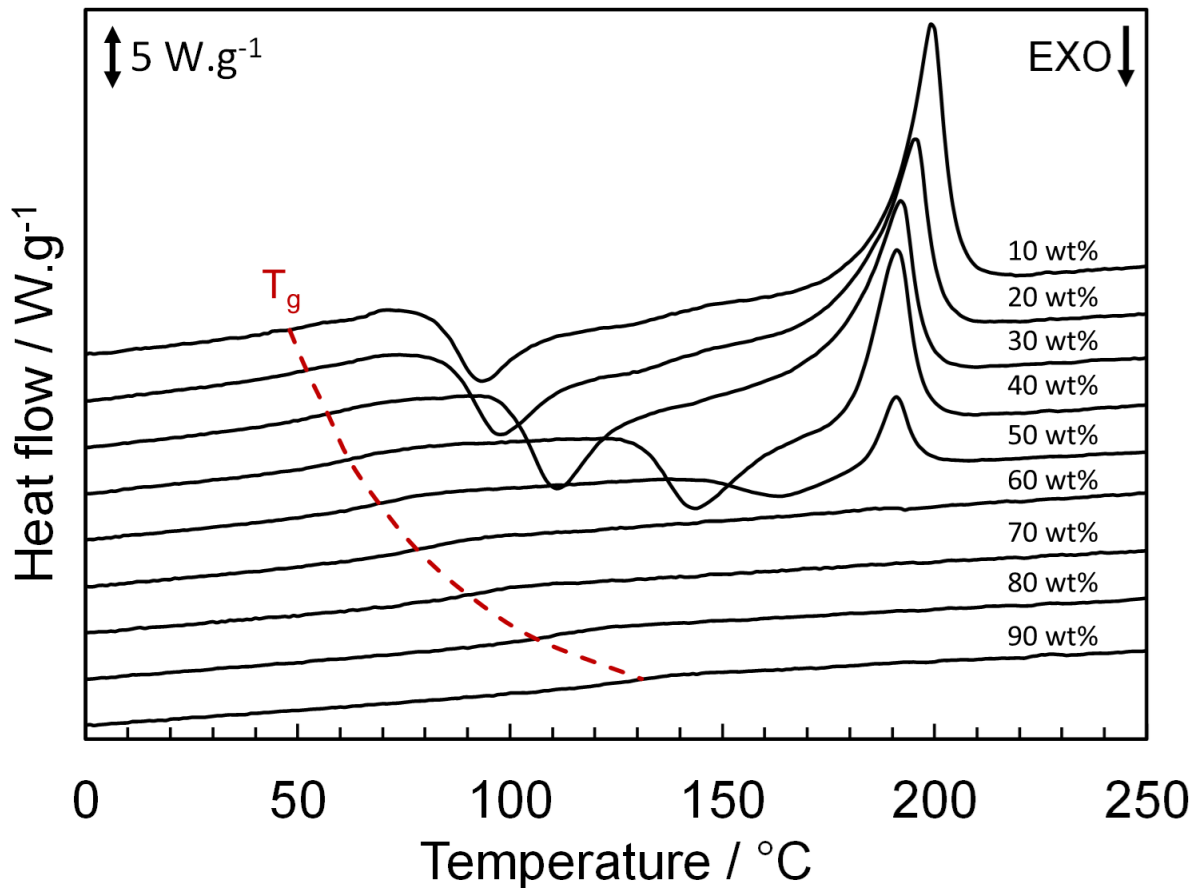


Figure 2: RHC heating curves of p-DTS(FBTTh₂)₂:PC₇₁BM mixtures after fast cooling from the melt (500 K.min⁻¹). The content of PC₇₁BM in each mixture is indicated on the right side of the curve. The red dashed line follows the evolution of T_g as a guide to the eye. The curves are shifted vertically proportional to the content of PC₇₁BM.

A model based on the Gordon-Taylor equation,⁴⁷ which fits the experimental data, is presented in Figure 4:

$$T_g = \frac{(w_1 T_{g1} + k_{GT} w_2 T_{g2})}{w_1 + k_{GT} w_2} \quad (1)$$

where 1 and 2 stand for p-DTS(FBTTh₂)₂ and PC₇₁BM, respectively, w is the weight fraction of each molecule, and k_{GT} is the Gordon-Taylor fitting parameter (k_{GT} = 0.235). The direct link between the T_g of the amorphous phase and its composition is a useful tool when studying mixtures after slow cooling and for establishing the p-DTS(FBTTh₂)₂:PC₇₁BM state diagram. Note that for this fitting procedure a single T_g value of 45 °C was used for p-DTS(FBTTh₂)₂.

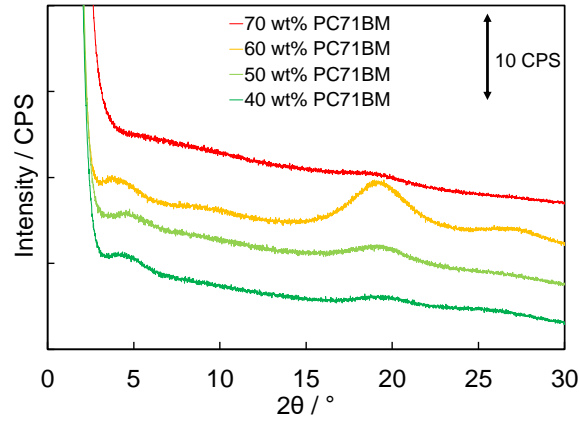


Figure 3: XRD diffractograms for p-DTS(FBTTh₂)₂:PC₇₁BM mixtures after quench cooling from the melt. The curves are shifted vertically for clarity.

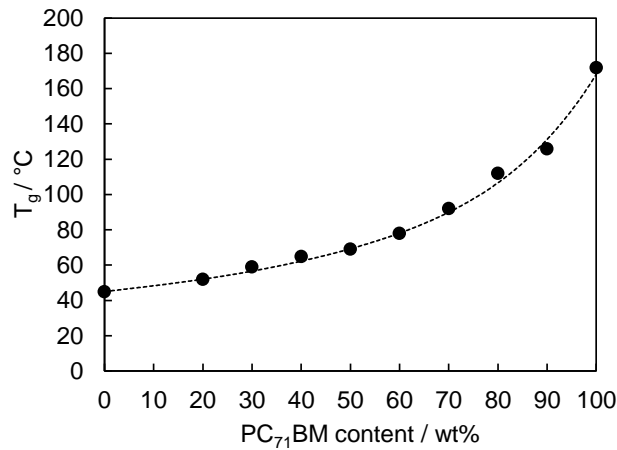


Figure 4: T_g as a function of composition for p-DTS(FBTTh₂)₂:PC₇₁BM mixtures after fast cooling (500 K.min⁻¹) from the melt (full black circles). The dashed line represents the Gordon-Taylor fit ($k_{GT} = 0.235$).

3.3. Characterization of the ordered phase by slow cooling of p-DTS(FBTTh₂)₂:PC₇₁BM mixtures

For the samples slowly cooled at 1 K.min⁻¹ from the melt, all mixtures with a PC₇₁BM content below 70 wt% exhibit a significant crystalline phase, as can be seen from the melting peaks in the thermograms, and which can be attributed to p-DTS(FBTTh₂)₂ crystals based on the position of the melting peak (Figure 5). No reorganization is observed upon heating at 500 K.min⁻¹. Both the enthalpic content and the maximum and endset (T_e) of the melting peak decrease with an increasing PC₇₁BM content, indicating less stable crystals and a reduced crystallinity for a higher PC₇₁BM concentration. This indicates the detrimental effect of PC₇₁BM on the crystallization kinetics of p-DTS(FBTTh₂)₂, even when samples are subjected to a very slow cooling to promote crystallization. When a threshold of 70 wt% of PC₇₁BM is reached, the absence of any melting transition indicates a completely disordered mixture, in agreement with XRD measurements (see below, Figure 6). Samples with 80 and 90 wt% PC₇₁BM are less reproducible (not shown in Figure 5), possibly due to liquid-liquid phase separation occurring during the slow cooling from the melt (see also as-cast mixtures in 3.4).

The XRD diffractograms of the slowly cooled mixtures below 70 wt% PC₇₁BM (Figure 6) show clear sharp diffraction peaks at $2\theta \approx 4^\circ$, 8° and 12° , associated with (001), (002), and (003) planes of alkyl chain stacking in p-DTS(FBTTh₂)₂ crystals, and at $2\theta \approx 25^\circ$ associated with π - π stacking in p-DTS(FBTTh₂)₂ crystals, respectively.^{16,18,20,23,25,48} The 2θ -range of 16 – 22° is often linked to amorphousness of either pure p-DTS(FBTTh₂)₂ or p-DTS(FBTTh₂)₂:PC₇₁BM mixtures.^{16,48} The presence of both intense sharp diffraction peaks and weak and broad signals confirms the semi-crystalline nature of the slowly cooled mixtures. The broad peak at $2\theta \approx 16 - 22^\circ$ associated with the presence of the amorphous phase gets more intense and diffraction peaks related to p-DTS(FBTTh₂)₂ crystals become less intense as the content of PC₇₁BM increases. The mixture with 70 wt% PC₇₁BM is completely amorphous according to XRD, confirming the measurement by RHC (Figure 5). Moreover, pure PC₇₁BM, when cooled at 1 K.min⁻¹, is (partially) ordered with clear diffraction peaks at $2\theta \approx 8.5^\circ$ and $2\theta \approx 10^\circ$ (see black curve, Figure 6).⁴⁹ However, these

characteristic diffraction peaks are absent in all mixtures. This indicates that PC₇₁BM, once mixed with p-DTS(FBTTh₂)₂, is completely amorphous. These observations show that the mixtures' crystallinity decreases with a higher content of PC₇₁BM and that only p-DTS(FBTTh₂)₂ crystals are present in the slowly cooled mixtures. This information is important for the quantification of the p-DTS(FBTTh₂)₂ melting peaks of Figure 5.

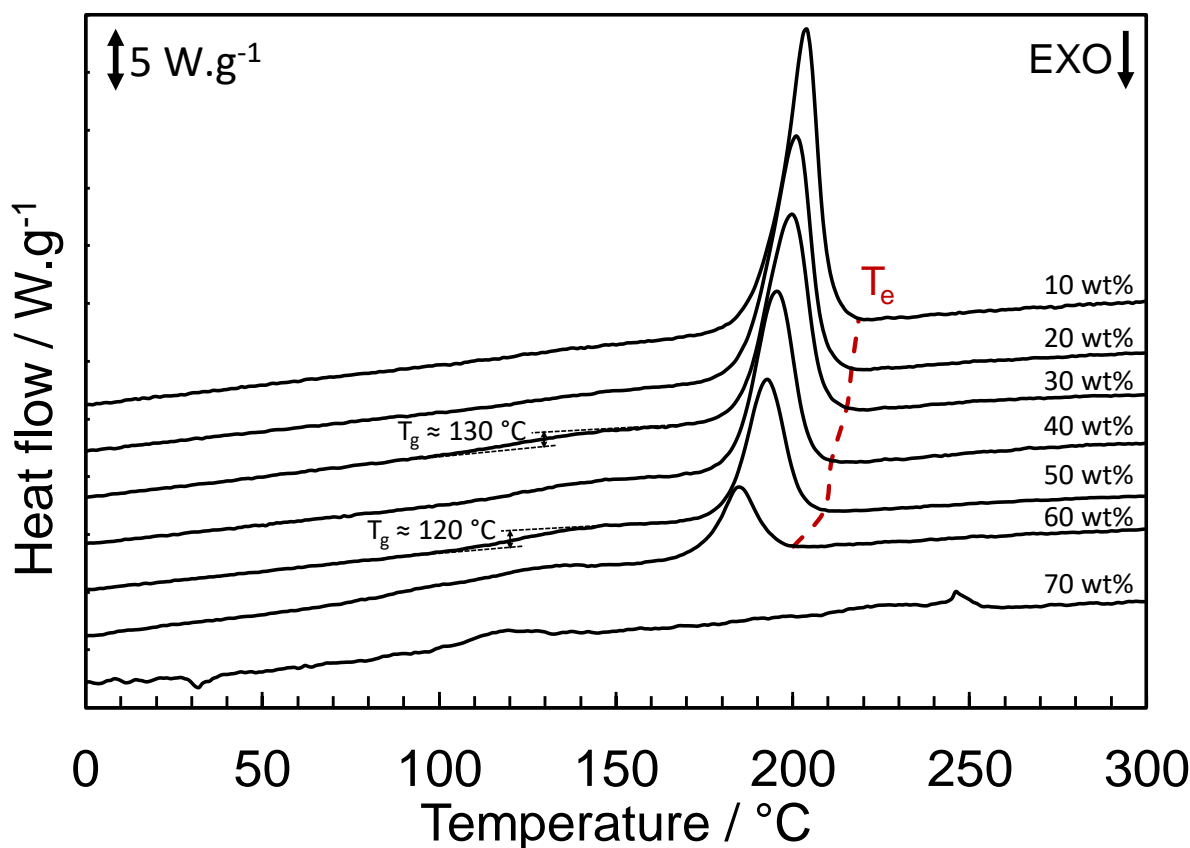


Figure 5: RHC heating curves of p-DTS(FBTTh₂)₂:PC₇₁BM mixtures after slow cooling (1 K.min⁻¹) from the melt. The content of PC₇₁BM in each mixture is indicated on the right side of the curves. The curves are shifted vertically for clarity.

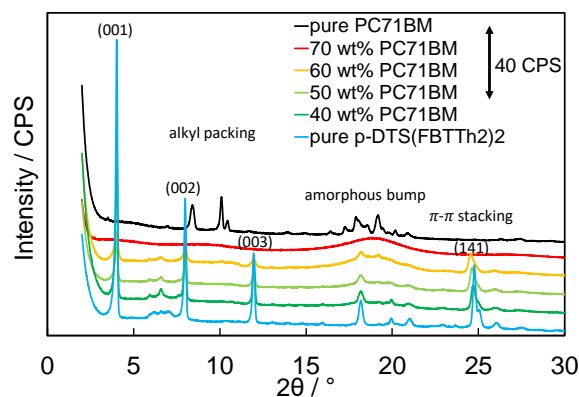


Figure 6: XRD diffractograms for p-DTS(FBTTh₂)₂:PC₇₁BM mixtures after slow cooling at 1 K.min⁻¹ from the melt. The curves are shifted vertically for clarity.

Figure 7 represents the evolution of the melting enthalpy of all mixtures of Figure 5. The black circles represent the observed experimental values, while the dashed line represents the expected calculated values based on the relative content of p-DTS(FBTTh₂)₂ in the mixtures with the assumption that crystallization of p-DTS(FBTTh₂)₂ is unhindered by the presence of PC₇₁BM in the amorphous phase. The expected values match closely for mixtures containing less than 40 wt% PC₇₁BM. From 40 wt% on, the experimentally observed ΔH_m is significantly below the expected value (indicated by the dashed line) and the difference widens up to 70 wt% PC₇₁BM where ΔH_m equals zero, demonstrating the strong effect of PC₇₁BM on p-DTS(FBTTh₂)₂ crystal formation. Note that this approach is based on the assumption that no PC₇₁BM crystals are formed in the mixtures and that the developed crystallinity is only due to p-DTS(FBTTh₂)₂ crystallization, as proven by the diffractograms of Figure 6 and also confirmed by ss-NMR (see 3.6.).

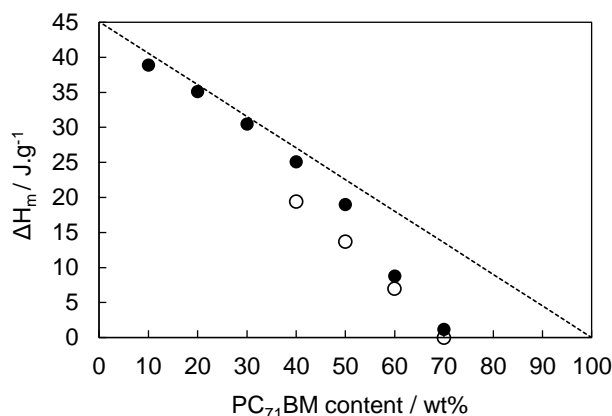


Figure 7: Experimental melting enthalpy measured by RHC (ΔH_m expressed per gram of mixture) as a function of composition (full circles) of p-DTS(FBTTh₂)₂:PC₇₁BM mixtures after slow cooling (1 K.min⁻¹) from the melt. The dashed line represents the expected (calculated) ΔH_m based on the p-DTS(FBTTh₂)₂ content in the mixture. The open circles represent ΔH_m values corresponding to the crystallinity calculated by ss-NMR (see 3.6.).

3.4. Development of the p-DTS(FBTTh₂)₂:PC₇₁BM state diagram

The findings on the amorphous and ordered phases of p-DTS(FBTTh₂)₂:PC₇₁BM mixtures can be combined to define a state diagram of both components. Note that none of the observed thermal transitions reflects a material under thermodynamic equilibrium. Hence, this diagram is called ‘state diagram’ instead of ‘phase diagram’ since the latter is associated to a system in thermodynamic equilibrium. The state diagram is presented in Figure 8. The onset of crystallization (T_c) (black diamonds Figure 8), and the corresponding endset of melting (full black circles in Figure 8) give information regarding the ordered phase.

The state diagram also displays T_g after fast cooling (red triangles in Figure 8) and slow cooling (full black triangles in Figure 8), which gives information regarding the mixed amorphous phase of fully amorphous and semi-crystalline p-DTS(FBTTh₂)₂:PC₇₁BM mixtures, respectively. The T_g of the semi-crystalline mixtures is difficult to detect (see Figure 5 for 30 and 50 wt% PC₇₁BM) due to the lower fraction of the amorphous phase. Due to crystallization of p-DTS(FBTTh₂)₂, the composition of the amorphous phase will be enriched in PC₇₁BM (staying fully amorphous) and therefore be different from the initial compositions of the fully amorphous samples. The resulting increase in T_g can be calculated according to the T_g -composition relationship of Figure 4 (Gordon-Taylor equation) in combination with the difference between the expected and measured ΔH_m values of Figure 7 (giving the amount of p-DTS(FBTTh₂)₂ remaining in the amorphous phase). A good

agreement between the measured and calculated T_g values is observed; the calculated values are depicted in Figure 8. The effect of the crystallization of p-DTS(FBTTh₂)₂ on the increase of T_g can clearly be seen (see arrow for 30 wt% PC₇₁BM in Figure 8), as well as how this effect reduces and eventually becomes non-existent when the crystallization process is fully inhibited at a PC₇₁BM content of 70 wt%.

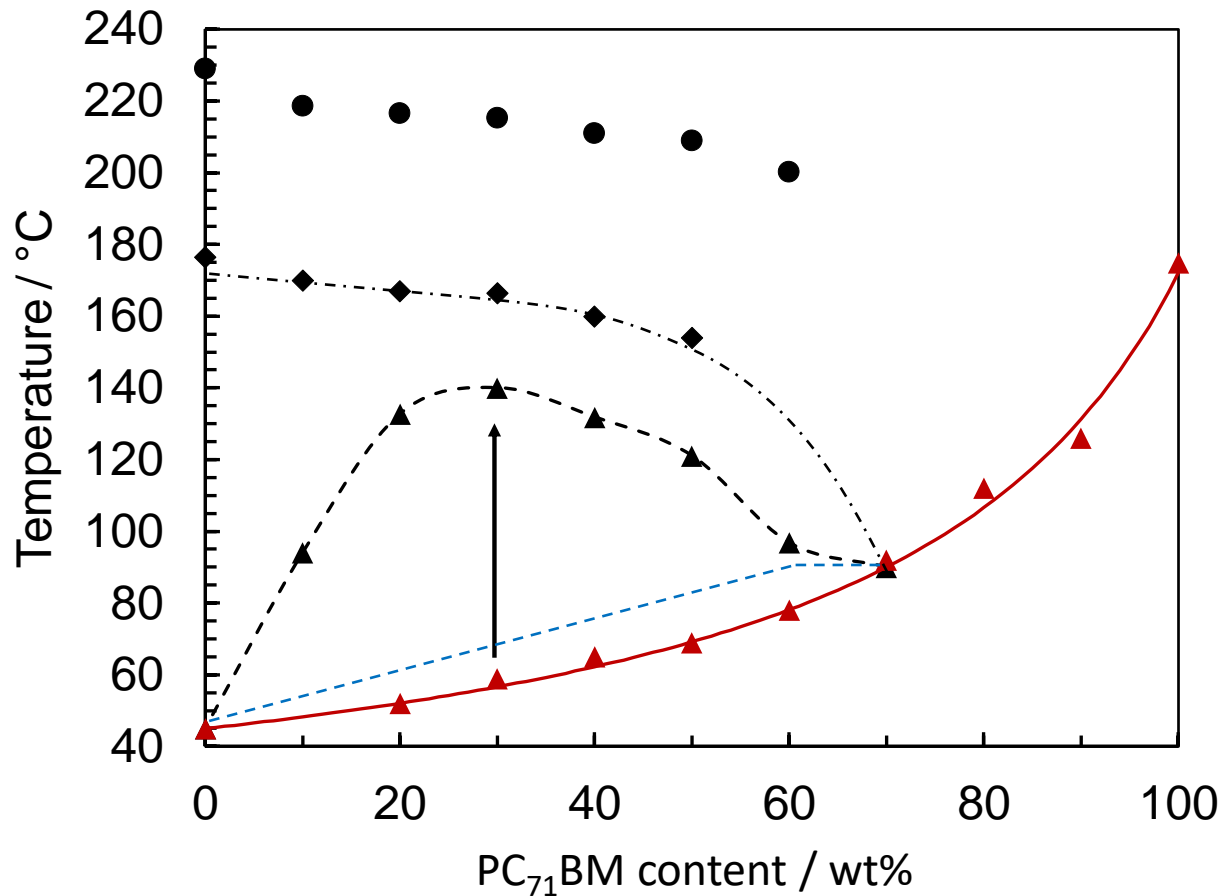


Figure 8: State diagram of p-DTS(FBTTh₂)₂:PC₇₁BM based on mixtures subjected to different thermal protocols. Full circles represent the endset of melting of mixtures measured after slow cooling (1 K.min⁻¹) from the melt. Black diamonds correspond to the onset of crystallization T_c in slow cooling (1 K.min⁻¹). The dash-dot black line follows and extrapolates the evolution of T_c towards higher PC₇₁BM content as guide to the eye. Full red triangles present the evolution of T_g after fast cooling (500 K.min⁻¹), which is also described by the T_g -composition relationship (solid red line). Full black triangles represent the calculated T_g of slowly cooled mixtures (see text), with a dashed black line as guide to the eye. An indication of the intermediate T_g trend for as-cast mixtures is also given (dashed blue line).

Starting at a total PC₇₁BM content around 40 wt%, the slower crystallization kinetics, coupled with the strongly increased T_g of the mixed amorphous phase, will eventually cause the crystallization during cooling to cease due to a lack of mobility of the amorphous phase, leading to partial crystallization ($\Delta H_m < \Delta H_{m,expected}$). This effect becomes more pronounced as the total PC₇₁BM content increases, until at ca. 70 wt% PC₇₁BM the mixture vitrifies before p-DTS(FBTTh₂)₂ can crystallize out of the melt (temperature-induced vitrification). This inhibiting effect of PC₇₁BM on the crystallization rate can be seen by extrapolating the T_c trend to mixtures with a higher content in PC₇₁BM (dash-dot line following the black diamonds, Figure 8). It explains the complete amorphousness around 70 wt% PC₇₁BM, driven by the vitrification of the mixed disordered phase of the slowly cooled mixtures. The state diagram is a powerful tool to understand the effect of different thermal treatments, and can be used to define appropriate thermal conditions to optimize the morphology of the active layer and hence to improve device efficiency.

3.5. Effect of the processing conditions in as-cast p-DTS(FBTTh₂)₂:PC₇₁BM mixtures

Processing conditions have a crucial impact on the morphology of the active layer, which strongly affects its opto-electronic properties and hence, device efficiency and stability. The RHC thermograms of the *first heating* (500 K.min⁻¹) after drop casting without thermal post-treatment are displayed in Figure 9. These samples most closely resemble the conditions of the mixtures used as active layers. In contrast with the samples with an additional thermal post-treatment (i.e. slow cooling from the melt), these first heating thermograms do show reorganization by cold crystallization. Most samples show a distinct melting peak, which is not entirely compensated by the preceding cold crystallization, indicative for the semi-crystalline nature after casting. This is confirmed by the XRD measurements depicted in Figure 10. Note that the diffractogram of the as-cast mixture with 70 wt% PC₇₁BM still shows a low crystallinity, in agreement with the thermogram in Figure 9. The observed semi-crystallinity is a result of the solvent casting procedure, which allows for more ordering compared to the quenching procedure, but clearly less than in the case of slow cooling. In the absence of a thermal post-treatment, the as-cast crystals are less perfect and even during fast heating at 500 K.min⁻¹ reorganization is interfering. After subtraction of the preceding cold crystallization enthalpy (ΔH_{cc}), the melting enthalpy (ΔH_m) after correction approaches the expected ΔH_m for the mixtures containing 40 wt% or less PC₇₁BM. This is in accordance

with the behavior seen for the slowly cooled mixtures (see §3.3, Fig. 7). As 40 wt% PC₇₁BM is the composition with the highest amount of PC₇₁BM for which all p-DTS(FBTTh₂)₂ is able to crystallize, and this is the composition leading to the most efficient devices,^{15,16,27} it may be hypothesized that this high efficiency is due to a combination of a crystalline p-DTS(FBTTh₂)₂ phase with a percolating mixed amorphous phase containing sufficient PC₇₁BM (see also §3.7).

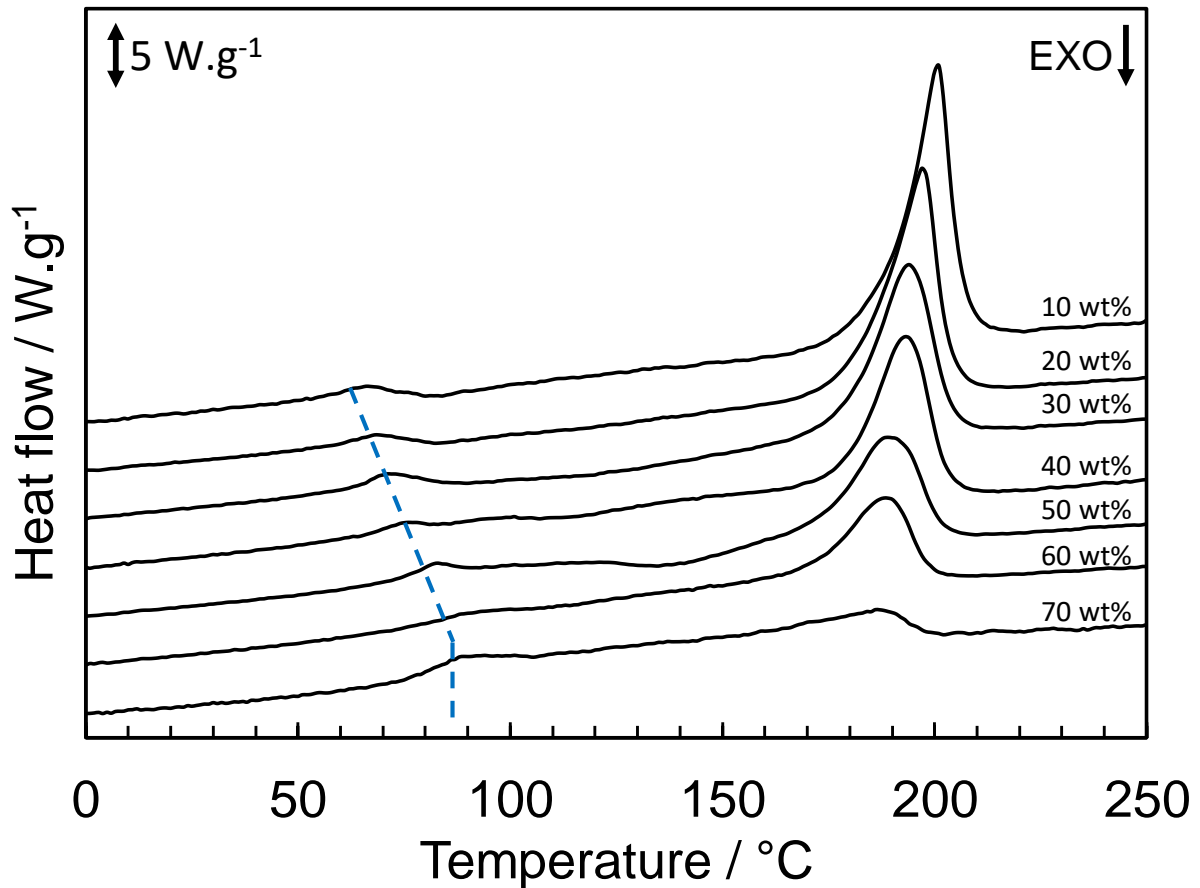


Figure 9: RHC heating curves of p-DTS(FBTTh₂)₂:PC₇₁BM mixtures at 500 K.min⁻¹ after casting (first heating). The content of PC₇₁BM in each mixture is indicated on the right side of the curve. The blue dashed line helps following the evolution of T_g as a function of mixture composition. The curves are shifted vertically for clarity.

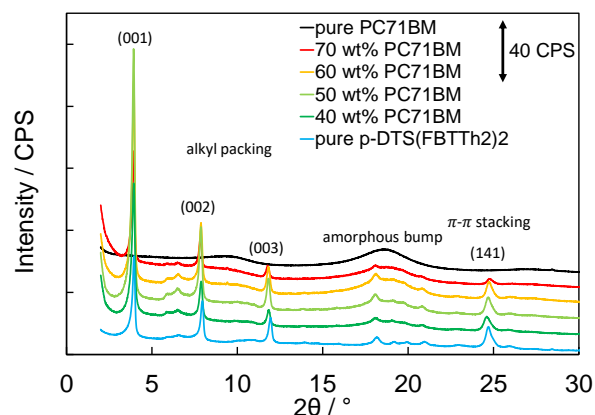


Figure 10: XRD diffractograms for p-DTS(FBTTh₂)₂:PC₇₁BM mixtures obtained after drop casting without further thermal treatment. The curves are shifted vertically for clarity.

Due to crystallization, the composition of the amorphous phase in the as-cast mixtures will again be enriched in PC₇₁BM. T_g is more easily detected than in the slowly cooled mixtures as the relative amount of amorphous material is higher. T_g of the drop casted mixtures shifts to higher temperatures as the PC₇₁BM content increases (see dashed line Figure 9), yielding an intermediate trend between the curves for rapidly and slowly cooled mixtures (see Figure 8). However, at compositions around 60-70 wt% PC₇₁BM, T_g remains constant at 90 °C and no longer increases with a higher PC₇₁BM content. As 90 °C is the temperature of the substrate on which casting and drying takes place, this puts an effective limit on the T_g of the mixtures. This can be explained by the T_g -composition relationship of Figure 4, where T_g of the mixtures can be seen to surpass 90 °C for compositions around 70 wt% PC₇₁BM. During drying, the T_g , which is lowered due to the plasticizing effect of the solvent, steadily increases as the solvent evaporates. When T_g of the mixture reaches the temperature of the substrate, the amorphous phase vitrifies and traps any remaining solvent, fixing the value of T_g at 90 °C.

3.6. ss-NMR characterization of p-DTS(FBTTh₂)₂:PC₇₁BM mixtures

To validate the previous findings and for a deeper insight into the morphology of all mixtures at the nanometer scale, proton wide-line ss-NMR relaxometry was used as a fast and non-invasive characterization method.^{37,50} Two relaxation time constants were investigated in particular, T_{1H} and $T_{1\rho H}$ (see 2.3 and ref. 40 for more details). The spin-lattice or T_{1H} relaxation (in the order of seconds) is dominated by the spectral density of (segmental) chain motions in the MHz region, while the spin-lattice relaxation in the rotating frame or $T_{1\rho H}$

relaxation (in the order of milliseconds) is mainly affected by slower motions in the kHz region. In solid systems, both decay times are influenced by the process of spin diffusion (SD), in contrast to the fast (in the order of μs) spin-spin or T_{2H} relaxation.⁵¹ Proton SD is not a physical movement of protons but a transfer of nuclear spin energy by successive energy-conserving nuclear spin flips. It allows to judge the degree of phase separation and to roughly estimate the size of phase-separated molecular domains. The maximum diffusive path length L can be approximated by the following Fickian diffusion equation:

$$L = (6 * D * T_{iH})^{1/2} \quad (2)$$

in which T_{iH} is the T_{1H} or $T_{1\rho H}$ relaxation decay time and D is the spin diffusion coefficient ($\sim 4\text{-}6 \times 10^{-16} \text{ m}^2 \text{ s}^{-1}$ for solid organic systems).^{52,53}

All the experimentally obtained relaxation times are summarized in Table 1 and the main conclusions are discussed below. Looking at the T_{1H}^L (i.e. the *Long* decay time) relaxation time of the drop casted samples without thermal post-treatment, it can be seen that the relaxation behavior is significantly closer to the shortest T_{1H}^L of the pure samples, i.e. that of p-DTS(FBTTh₂)₂. This indicates that the magnetization of all the excited proton spins can diffuse to a p-DTS(FBTTh₂)₂ molecule, where they quickly relax to the ground state. This implies closely mixed systems on a 50 nm scale as determined by the spin diffusion equation (2) on the T_{1H} time scale. The slower T_{1H}^L relaxation (longer decay) time with increasing PC₇₁BM content can be attributed to an increase of the amorphous character (as the quenched samples appear to have a longer T_{1H}^L compared to the slowly cooled samples). Only in the case of pure PC₇₁BM, the T_{1H}^L relaxation time increases significantly and a second, even longer contribution (6.34 s) appears upon slow cooling. This is due to the formation of large crystalline domains, not present in quenched or as-cast PC₇₁BM neither in any other mixture. This is a confirmation that PC₇₁BM is amorphous when mixed with p-DTS(FBTTh₂)₂, as also indicated by XRD.

In the case of $T_{1\rho H}^L$, an average value is observed for the mixtures, based on the relaxation time of the pure components, weighted for their respective contribution to the total amount of protons in the mixture. Assuming all material in the quenched mixtures is amorphous, which was confirmed by RHC and XRD, we can calculate the actual contribution to the relaxation pathway of the quenched mixtures as a linear combination of the relaxation constants of the pure amorphous components:

$$T_{1\rho H}L_{(\text{quenched})} = x * T_{1\rho H}L_{(\text{p-DTS(FBTTh}_2)_2 - \text{quenched})} + y * T_{1\rho H}L_{(\text{PC}_{71}\text{BM} - \text{quenched})} \quad (3)$$

with x:y the composition of the p-DTS(FBTTh₂)₂:PC₇₁BM mixture (x + y = 1).

Assuming that all the PC₇₁BM in the mixture is amorphous and assuming the relative contribution of the two components to the relaxation is independent of the casting conditions, the relative composition of the crystalline and amorphous p-DTS(FBTTh₂)₂ (fractions a and b, respectively) in the drop casted or slowly cooled mixtures can be calculated as follows:

$$T_{1\rho H}L_{(\text{drop casted/slowly cooled})} = a * T_{1\rho H}L_{(\text{p-DTS(FBTTh}_2)_2 - \text{slowly cooled})} + b * T_{1\rho H}L_{(\text{p-DTS(FBTTh}_2)_2 - \text{quenched})} + y * T_{1\rho H}L_{(\text{PC}_{71}\text{BM} - \text{quenched})} \quad (4)$$

with a + b = x.

The calculated crystallinity of p-DTS(FBTTh₂)₂ based on the $T_{1\rho H}L$ data is shown in Table 2. In agreement with RHC and XRD results, p-DTS(FBTTh₂)₂ is less crystalline if the PC₇₁BM content is increased, and in case of 70 wt% PC₇₁BM the crystallinity of the mixture drops to zero. The crystallinity is also higher in slowly cooled samples than in drop casted samples without further thermal treatment. If the calculated ss-NMR crystallinity is converted to a calculated ΔH_m (by using the expected ΔH_m for the different mixtures as defined in 3.3, see Figure 7), a comparison can be made with the experimental RHC measurements. The calculated ΔH_m values according to ss-NMR (open circles in Figure 7) are somewhat lower than the experimental RHC data. This difference might be due to the assumption that quench-cooled p-DTS(FBTTh₂)₂ is fully amorphous, while some evidence exists it may be up to 10% crystalline.³⁰ A truly amorphous p-DTS(FBTTh₂)₂ mixture would yield an even shorter $T_{1\rho H}L$ relaxation time, leading to a higher calculated crystallinity and a closer agreement with RHC data. Additionally, the physical properties measured and the concepts used to express a certain degree of order with RHC (heat flow and the latent enthalpy of melting associated with enthalpic interactions) and ss-NMR (relaxation time of excited proton spins) are different. Therefore, a perfect match of the crystallinity given by the two techniques should not be expected. More specifically, crystal (im)perfection and the occurrence of nano-sized crystals probably have a different effect on the quantification of crystallinity using both techniques. Despite this difference in crystallinity, both techniques indicate the same effect of PC₇₁BM in the mixtures, i.e. the hindrance leading to complete inhibition of p-DTS(FBTTh₂)₂ crystallization at 70 wt% PC₇₁BM.

Table 1: Proton wide-line ss-NMR relaxometry data for drop casted, quenched and slowly cooled p-DTS(FBTTh₂)₂:PC₇₁BM mixtures. ‘S’ and ‘L’ refer to the fractions (%) with short, and long decay time, respectively.

DTS(FBTTh ₂) ₂ : PC ₇₁ BM (wt%:wt%)	$T_{1\rho}^S$ (s)			$T_{1\rho}^L$ (s)			$T_{1\rho}^S$ (ms)			$T_{1\rho}^L$ (ms)		
	Drop casted	Quenched	Slowly cooled	Drop casted	Quenched	Slowly cooled	Drop casted	Quenched	Slowly cooled	Drop casted	Quenched	Slowly cooled
100:0	0.09 4%	0.12 4%	0.14 11%	0.98 96%	1.08 96%	1.02 89%	1.14 26%	0.99 28%	0.97 25%	6.18 74%	3.31 72%	6.53 75%
0:100	0.12 10%	0.30 28%	0.13 14%	2.38 90%	1.21 72%	1.96 46% 6.34 41%	1.43 31%	1.25 31%	1.18 31%	12.38 70%	14.24 69%	13.1 69%
60:40	0.13 6.7%	0.17 8.5%	0.13 17.2%	1.07 93%	1.14 92%	1.06 83%	1.39 35%	1.14 27%	0.98 32%	7.56 66%	6.98 73%	8.00 67%
50:50	0.14 7%	0.12 8%	0.14 11%	1.09 93%	1.16 92%	1.06 89%	1.52 32%	1.30 27%	1.27 32%	8.56 67%	8.20 73%	8.75 68%
40:60	0.17 9%	0.14 16%	0.15 11%	1.15 91%	1.20 84%	1.08 90%	1.42 30%	0.94 29%	1.39 34%	9.42 70%	9.10 71%	9.72 66%
30:70	0.14 11%	0.13 11%	0.14 12%	1.26 91%	1.18 90%	1.13 88%	1.50 29%	1.18 25%	1.27 28%	11.00 71%	11.20 75%	11.09 72%

Table 2: Crystalline fraction of p-DTS(FBTTh₂)₂ in p-DTS(FBTTh₂)₂:PC₇₁BM mixtures as calculated from $T_{1\rho}^L$ data.

DTS(FBTTh ₂) ₂ :PC ₇₁ BM (wt%:wt%)	Crystalline DTS(FBTTh ₂) ₂ fraction (%)	
	Drop casted	Slowly cooled
60:40	56	75
50:50	49	59
40:60	17	37
30:70	0	0

3.7. Effect of the processing additive DIO on p-DTS(FBTTh₂)₂:PC₇₁BM 60:40 mixtures

Since for the p-DTS(FBTTh₂)₂:PC₇₁BM system a 60:40 ratio is considered to give rise to the most efficient devices,¹⁶ this mixing ratio was chosen to study the effect of DIO as additive or co-solvent on the phase transitions. p-DTS(FBTTh₂)₂:PC₇₁BM 60:40 mixtures with 0.4 vol% of DIO were prepared following the solution processing conditions as defined in 2.4. The samples were subsequently dried in vacuum (3×10^{-7} mbar) for 2 hours to eliminate DIO. RHC thermograms comparing as-cast and slowly cooled p-DTS(FBTTh₂)₂:PC₇₁BM 60:40

mixtures with and without 0.4 vol% DIO are shown in Figure 11. DIO has a clear effect on both the crystalline and the amorphous phase, in the as-cast and even in the slowly cooled mixtures, despite the vacuum treatment. It indicates that DIO has a long-lasting and probably permanent effect on the mixture's thermal properties. These observations are in agreement with previous findings.²⁸

The as-cast as well as the slowly cooled mixtures display cold crystallization when DIO is used, even though the effect is somewhat less pronounced in the second heating. This is in contrast to the mixtures without DIO, where cold crystallization is absent after slow cooling at 1 K.min⁻¹ (see 3.3.). This indicates that the presence of DIO leads to slower crystallization kinetics in the cooling step. In addition, the co-solvent has a negative effect on the crystallinity of p-DTS(FBTTh₂)₂ since ΔH_m is lower in comparison with the mixture processed without DIO (see Figure 11), both in first (17.5 J.g⁻¹ with DIO versus 24.9 J.g⁻¹ without DIO, i.e. a drop of ca. 30% in crystallinity) and second heating (20.5 J.g⁻¹ with DIO versus 25.1 J.g⁻¹ without DIO, i.e. ca. 20% less crystalline). These RHC results are in contrast with literature reports that DIO increases the crystallinity compared to as-cast mixtures.¹⁶ It is known that DIO leads to relatively smaller crystals compared to a thermal post-treatment without DIO,¹⁶ and that this modified crystal size seems to be linked to a better device efficiency.^{15,16} The smaller crystal size seems to be confirmed by a lower T_m of p-DTS(FBTTh₂)₂ and a broader melting peak with a low-temperature tail for mixtures with DIO (see Figure 11). This is most likely due to less stable, less perfect crystals of p-DTS(FBTTh₂)₂ as a result of the lower crystallization rate induced by DIO in the cooling (also evidenced by the presence of cold crystallization in heating). It means that more p-DTS(FBTTh₂)₂ is present in the mixed amorphous phase if mixtures are subjected to the same cooling or drying treatment. The mixed amorphous phase together with the p-DTS(FBTTh₂)₂ crystals is crucial to maximize the interfacial area between donor and acceptor materials in a percolated morphology. The amount of crystals (crystallinity) must be high enough for a percolating pathway, but crystal size should not be too large to avoid charge recombination and reduction of interfacial area. Therefore, the combination of both a mixed amorphous phase promoting charge separation and a crystalline phase with relatively smaller crystals (but in a sufficient amount) conveying charges to their respective electrodes once separated could explain the higher performance of devices made of an active layer prepared with DIO. In case the thermal treatment stays identical as for the mixtures without DIO, the RHC results show that DIO has a negative effect on the mixture's crystallinity and on the rate of

crystallization of p-DTS(FBTTh₂)₂, with formation of less perfect crystals compared to mixtures prepared without DIO. These RHC results suggest that an ‘optimized’ effect of DIO can probably be reached by a dedicated thermal post-treatment to enhance the crystallinity, while maintaining appropriate crystal size(s) of p-DTS(FBTTh₂)₂.

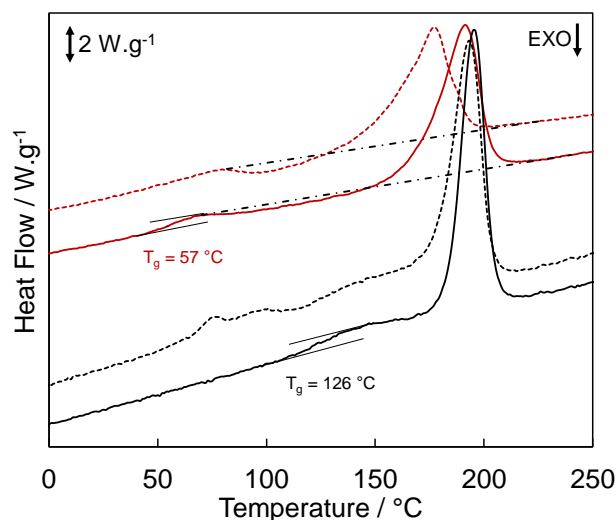


Figure 11: RHC heating curves of p-DTS(FBTTh₂)₂:PC₇₁BM 60:40 prepared with DIO (top curves, red) or without DIO (bottom curves, black). Dashed and solid curves represent the heating curves after drop casting and slow cooling at 1 K.min⁻¹, respectively.

DIO leads to a strong plasticizing effect, decreasing T_g of the mixed amorphous phase significantly. The plasticizing effect is more evident in the slowly cooled mixture as T_g is more easily defined due the much smaller enthalpic content of the following cold crystallization. The T_g of the mixed amorphous phase prepared with DIO after slow cooling lies ca. 70 °C lower than without DIO (T_g drops from 126 °C to 57 °C, see Figure 11). The experimental value of 57 °C is even lower than for the fully amorphous p-DTS(FBTTh₂)₂:PC₇₁BM 60:40 mixture after quench cooling (65 °C, see Figure 4), which clearly indicates that DIO plasticizes the mixture in two ways: (i) *directly*, by increasing the mobility of the disordered phase; (ii) *indirectly*, by lowering the ability of p-DTS(FBTTh₂)₂ to crystallize and leaving more p-DTS(FBTTh₂)₂ in the mixed amorphous phase. This indicates that adding DIO is detrimental for the thermal stability of the active layer. The morphology can reorganize towards a more thermodynamically stable form by coarsening at working temperatures higher than T_g , which could harm device efficiency and should therefore be avoided. As an OPV device can be subjected to temperatures up to 85 °C, a T_g higher than 57 °C for the mixed amorphous phase is desirable.³⁰

These RHC results suggest that optimizing the morphology, and hence device efficiency, by using DIO without a dedicated thermal post-treatment leads to a less thermally stable and less ordered active layer compared to DIO-free mixtures. Moreover, these results show that the ‘optimization’ of the ordered phase by using a co-solvent impacts the disordered mixed phase and decreases its stability. This yields a less stable mixture, which leads to an undesired morphology by coarsening and ultimately to a device of lower efficiency. One way to avoid such issues would be to develop dedicated post-thermal treatments that could mimic the beneficial effects of DIO on morphology.

3.8. Thermal post-treatment leading to additive-free p-DTS(FBTTh₂)₂:PC₇₁BM 60:40 mixtures

Devices with 40 wt% PC₇₁BM show the highest efficiency using conventional processing conditions. Therefore, a content of at least 40 wt% PC₇₁BM seems sufficient to provide the desired percolating morphology of the mixed amorphous phase (containing PC₇₁BM and p-DTS(FBTTh₂)₂) in combination with the p-DTS(FBTTh₂)₂ crystalline phase. A thermal annealing performed on mixtures prepared without DIO can promote ordering and efficiency if appropriate temperature and time conditions are chosen. Based on literature, a temperature of 130 °C applied for 10 min gave the best efficiency (5.8% without DIO, investigated temperature range 70-130 °C).¹⁶ Figure 9 (after casting) and Figure 2 (after fast cooling) indicate that in case of 40 wt% PC₇₁BM cold crystallization starts beyond ca. 75 °C and ca. 125 °C, respectively. If the same mixture is slowly cooled at 1 K.min⁻¹ from the melt, the crystallization trajectory during cooling is ca. 140-160 °C (see Figure 8). Moreover, T_g of the fully amorphous p-DTS(FBTTh₂)₂:PC₇₁BM 60:40 mixture lies at 65 °C, but rises to 126 °C in combination with p-DTS(FBTTh₂)₂ crystals melting at 211 °C after slow cooling (see Figure 8). This shows there is a high potential to improve active layers prepared without DIO by introducing a dedicated thermal post-treatment. The following DIO-free thermal treatment could be proposed: (i) Solution casting of a 40 wt% PC₇₁BM mixture of the highest possible amorphousness (e.g. by a fast evaporation process); (ii) The as-cast mixture should then be heated at a temperature just above T_g (lower limit: red triangle in Figure 8) to develop relatively small crystals, as the mobility of the mixture is low and the tendency for crystal nucleation is high in that temperature range; (iii) The temperature should then be increased at a rate evolving with the rising T_g during crystallization to avoid crystallization-induced

vitrification, till a final temperature at which the desired crystallinity and morphology is reached. The heating rate, depending on the crystallization kinetics of p-DTS(FBTTh₂)₂, and the upper temperature of thermal annealing (depending on optimized morphology and efficiency) should be determined experimentally (beyond the scope of this paper).

4. Conclusions

A comprehensive study of p-DTS(FBTTh₂)₂:PC₇₁BM mixtures was undertaken, using dedicated thermal protocols to investigate specifically the mixed amorphous phase, the crystalline/ordered phase, or the phases expected in as-cast mixtures, leading to the development of a state diagram. The effects of DIO as a processing additive on the most efficient mixture composition were also investigated. Rapid Heat-Cool differential scanning calorimetry (RHC) was proven to be a well-suited thermal analysis technique for these characterization purposes (see also Introduction).

When structure formation was avoided through fast cooling, it was possible to define the T_g-composition relationship for p-DTS(FBTTh₂)₂:PC₇₁BM mixtures, which could be described by the Gordon-Taylor equation. Knowledge of T_g is important, as this is the temperature above which thermal stability is compromised and reordering can take place.

On the other hand, a slow cooling was used to promote structure formation in these mixtures. Quantitative thermal analysis together with XRD and ss-NMR analysis proved that PC₇₁BM remained amorphous when mixed with p-DTS(FBTTh₂)₂. Moreover, the ability of p-DTS(FBTTh₂)₂ to crystallize is greatly influenced by the (changing) composition of the amorphous phase. As a consequence of p-DTS(FBTTh₂)₂ crystallization, the mixed amorphous phase is enriched in PC₇₁BM, causing T_g to increase. In combination with the slower p-DTS(FBTTh₂)₂ crystallization kinetics, this can lead to vitrification of the mixed amorphous phase before crystallization if the total amount of PC₇₁BM exceeds 70 wt%.

When mixtures were investigated which underwent the same solution processing as OPV active layers, the phase behavior could be explained by the information of the amorphous and ordered phases as limiting cases. p-DTS(FBTTh₂)₂ crystals were present to a lesser extent than in slowly cooled mixtures, and cold crystallization occurred upon heating. It was found that 40 wt% PC₇₁BM was the composition with the highest amount of PC₇₁BM that still allowed the p-DTS(FBTTh₂)₂ phase to fully crystallize, and this is also the most efficient composition according to literature, which may be explained by the combination of p-

DTS(FBTTh₂)₂ crystals and a mixed amorphous phase with a sufficient amount of PC₇₁BM that can lead to a percolating morphology. The observed evolution of T_g could be explained through the combination of the T_g-composition relationship and the conditions of specific solution processing and drying after casting. All information of the three dedicated thermal protocols is summarized in a state diagram for p-DTS(FBTTh₂)₂:PC₇₁BM, which is a valuable tool to predict the phase behavior in a systematic way.

When 0.4 vol% DIO was added as a processing additive, a significant influence on the phase behavior could be observed. DIO was found to remain in the mixture after a dedicated drying step under vacuum, and was found to affect the phase behavior even in a second heating after a slow cooling. According to RHC results, DIO leads to a lower crystallinity of p-DTS(FBTTh₂)₂, as well as a smaller average crystal size. Even more importantly, DIO acts as a strong plasticizer, lowering T_g significantly and thus the morphological stability of the p-DTS(FBTTh₂)₂:PC₇₁BM mixtures. Finally, an additive-free thermal annealing procedure was proposed, based on a slowly increasing annealing temperature, slightly above T_g, with the aim of obtaining smaller p-DTS(FBTTh₂)₂ crystals as well as sufficient crystallinity. The developed characterization methodology is expandable to other small molecule organic bulk heterojunction systems.

Acknowledgements

The authors acknowledge the financial support of the Agency for Innovation by Science and Technology (IWT) (PhD fellowship M.D.), and the Research Foundation – Flanders (FWO-Vlaanderen) (project G0B2718N and postdoctoral fellowship P.V.). The XRD measurements were performed by Bart Ruttens in the group of Prof. Jan D’Haen at Hasselt University. This work is supported by Hasselt University and the Research Foundation Flanders (FWO-Vlaanderen; Hercules project GOH3816NAUHL).

References

- (1) Brabec, C. J.; Gowrisanker, S.; Halls, J. J. M.; Laird, D.; Jia, S.; Williams, S. P. Polymer-Fullerene Bulk-Heterojunction Solar Cells. *Adv. Mater.* **2010**, 22 (34), 3839–3856.
- (2) Etxebarria, I.; Ajuria, J.; Pacios, R. Solution-Processable Polymeric Solar Cells: A Review on Materials, Strategies and Cell Architectures to Overcome 10%. *Org. Electron.* **2015**, 19, 34–60.

- (3) Huang, Y.; Kramer, E. J.; Heeger, A. J.; Bazan, G. C. Bulk Heterojunction Solar Cells: Morphology and Performance Relationships. *Chem. Rev.* **2014**, *114* (14), 7006–7043.
- (4) Holliday, S.; Li, Y.; Luscombe, C. K. Recent Advances in High Performance Donor-Acceptor Polymers for Organic Photovoltaics. *Prog. Polym. Sci.* **2017**, *70*, 34–51.
- (5) Yan, C.; Barlow, S.; Wang, Z.; Yan, H.; Jen, A. K. Y.; Marder, S. R.; Zhan, X. Non-Fullerene Acceptors for Organic Solar Cells. *Nat. Rev. Mater.* **2018**, *3* (3), 18003.
- (6) Fan, B.; Zhang, D.; Li, M.; Zhong, W.; Zeng, Z.; Ying, L.; Huang, F.; Cao, Y. Achieving over 16% Efficiency for Single-Junction Organic Solar Cells. *Sci. China Chem.* **2019**, *62* (6), 746–752.
- (7) Collins, S. D.; Ran, N. A.; Heiber, M. C.; Nguyen, T.-Q. Small Is Powerful: Recent Progress in Solution-Processed Small Molecule Solar Cells. *Adv. Energy Mater.* **2017**, *7* (10), 1602242.
- (8) Ni, W.; Wan, X.; Li, M.; Wang, Y.; Chen, Y. A–D–A Small Molecules for Solution-Processed Organic Photovoltaic Cells. *Chem. Commun.* **2015**, *51* (24), 4936–4950.
- (9) Fan, H.; Zhu, X. Development of Small-Molecule Materials for High-Performance Organic Solar Cells. *Sci. China Chem.* **2015**, *58* (6), 922–936.
- (10) Deng, D.; Zhang, Y.; Zhang, J.; Wang, Z.; Zhu, L.; Fang, J.; Xia, B.; Wang, Z.; Lu, K.; Ma, W.; *et al.* Fluorination-Enabled Optimal Morphology Leads to over 11% Efficiency for Inverted Small-Molecule Organic Solar Cells. *Nat. Commun.* **2016**, *7* (1), 13740.
- (11) Huo, Y.; Zhang, H.-L.; Zhan, X. Nonfullerene All-Small-Molecule Organic Solar Cells. *ACS Energy Lett.* **2019**, *4* (6), 1241–1250.
- (12) Vangerven, T.; Verstappen, P.; Drijkoningen, J.; Dierckx, W.; Himmelberger, S.; Salleo, A.; Vanderzande, D.; Maes, W.; Manca, J. V. Molar Mass versus Polymer Solar Cell Performance: Highlighting the Role of Homocouplings. *Chem. Mater.* **2015**, *27* (10), 3726–3732.
- (13) Verstappen, P.; Cardinaletti, I.; Vangerven, T.; Vanormelingen, W.; Verstraeten, F.; Lutsen, L.; Vanderzande, D.; Manca, J.; Maes, W. Impact of Structure and Homo-Coupling of the Central Donor Unit of Small Molecule Organic Semiconductors on

- Solar Cell Performance. *RSC Adv.* **2016**, 6 (38), 32298–32307.
- (14) Pirotte, G.; Verstappen, P.; Vanderzande, D.; Maes, W. On the “True” Structure of Push-Pull-Type Low-Bandgap Polymers for Organic Electronics. *Adv. Electron. Mater.* **2018**, 4 (10), 1700481.
- (15) van der Poll, T. S.; Love, J. A.; Nguyen, T.-Q.; Bazan, G. C. Non-Basic High-Performance Molecules for Solution-Processed Organic Solar Cells. *Adv. Mater.* **2012**, 24 (27), 3646–3649.
- (16) Love, J. A.; Proctor, C. M.; Liu, J.; Takacs, C. J.; Sharenko, A.; Van Der Poll, T. S.; Heeger, A. J.; Bazan, G. C.; Nguyen, T. Q. Film Morphology of High Efficiency Solution-Processed Small-Molecule Solar Cells. *Adv. Funct. Mater.* **2013**, 23 (40), 5019–5026.
- (17) Kyaw, A. K. K.; Wang, D. H.; Luo, C.; Cao, Y.; Nguyen, T.-Q.; Bazan, G. C.; Heeger, A. J. Effects of Solvent Additives on Morphology, Charge Generation, Transport, and Recombination in Solution-Processed Small-Molecule Solar Cells. *Adv. Energy Mater.* **2014**, 4 (7), 1301469.
- (18) Perez, L. A.; Chou, K. W.; Love, J. A.; van der Poll, T. S.; Smilgies, D.-M.; Nguyen, T.-Q.; Kramer, E. J.; Amassian, A.; Bazan, G. C. Solvent Additive Effects on Small Molecule Crystallization in Bulk Heterojunction Solar Cells Probed During Spin Casting. *Adv. Mater.* **2013**, 25 (44), 6380–6384.
- (19) Engmann, S.; Bokel, F. A.; Herzog, A. A.; Ro, H. W.; Girotto, C.; Caputo, B.; Hoven, C. V.; Schaible, E.; Hexemer, A.; DeLongchamp, D. M.; *et al.* Real-Time X-Ray Scattering Studies of Film Evolution in High Performing Small-Molecule–Fullerene Organic Solar Cells. *J. Mater. Chem. A* **2015**, 3 (16), 8764–8771.
- (20) Herath, N.; Das, S.; Keum, J. K.; Zhu, J.; Kumar, R.; Ivanov, I. N.; Sumpter, B. G.; Browning, J. F.; Xiao, K.; Gu, G.; *et al.* Peculiarity of Two Thermodynamically-Stable Morphologies and Their Impact on the Efficiency of Small Molecule Bulk Heterojunction Solar Cells. *Sci. Rep.* **2015**, 5 (1), 13407.
- (21) Kyaw, A. K. K.; Wang, D. H.; Wynands, D.; Zhang, J.; Nguyen, T.-Q.; Bazan, G. C.; Heeger, A. J. Improved Light Harvesting and Improved Efficiency by Insertion of an Optical Spacer (ZnO) in Solution-Processed Small-Molecule Solar Cells. *Nano Lett.*

- 2013**, *13* (8), 3796–3801.
- (22) Chen, Y.; Zhang, X.; Zhan, C.; Yao, J. In-Depth Understanding of Photocurrent Enhancement in Solution-Processed Small-Molecule:Perylene Diimide Non-Fullerene Organic Solar Cells. *Phys. status solidi* **2015**, *212* (9), 1961–1968.
 - (23) Karak, S.; Liu, F.; Russell, T. P.; Duzhko, V. V. Bulk Charge Carrier Transport in Push–Pull Type Organic Semiconductor. *ACS Appl. Mater. Interfaces* **2014**, *6* (23), 20904–20912.
 - (24) Sharenko, A.; Treat, N. D.; Love, J. A.; Toney, M. F.; Stingelin, N.; Nguyen, T. Use of a Commercially Available Nucleating Agent to Control the Morphological Development of Solution-Processed Small Molecule Bulk Heterojunction Organic Solar Cells. *J. Mater. Chem. A* **2014**, *2* (38), 15717–15721.
 - (25) Luo, D.; Man, J.; Yu, L.; Liu, Z.; Peng, J.; Shi, G.; Zhu, X.; Ma, W. Thermal-Annealing Dependence of Crystallization on Solution-Processed Small-Molecule Organic Photovoltaics. *Phys. Status Solidi Appl. Mater. Sci.* **2016**, *213* (2), 412–418.
 - (26) Zhou, W.; Xie, Y.; Hu, X.; Zhang, L.; Meng, X.; Zhang, Y.; Ma, W.; Chen, Y. Surface Treatment by Binary Solvents Induces the Crystallization of a Small Molecular Donor for Enhanced Photovoltaic Performance. *Phys. Chem. Chem. Phys.* **2015**, *18*, 735–742.
 - (27) Abdelsamie, M.; Treat, N. D.; Zhao, K.; McDowell, C.; Burgers, M. A.; Li, R.; Smilgies, D. M.; Stingelin, N.; Bazan, G. C.; Amassian, A. Toward Additive-Free Small-Molecule Organic Solar Cells: Roles of the Donor Crystallization Pathway and Dynamics. *Adv. Mater.* **2015**, *27* (45), 7285–7292.
 - (28) Vangerven, T.; Verstappen, P.; Patil, N.; D’Haen, J.; Cardinaletti, I.; Benduhn, J.; Van den Brande, N.; Defour, M.; Lemaire, V.; Beljonne, D.; *et al.* Elucidating Batch-to-Batch Variation Caused by Homocoupled Side Products in Solution-Processable Organic Solar Cells. *Chem. Mater.* **2016**, *28* (24), 9088–9098.
 - (29) Van den Brande, N.; Defour, M.; Liu, Z.; Verstappen, P.; Nies, E.; Maes, W.; Van Assche, G.; Van Mele, B. Homocoupling Defects of a Small Donor Molecule for Organic Photovoltaics: Quantification of the Eutectic State Diagram by Rapid Heat–Cool Differential Scanning Calorimetry. *J. Phys. Chem. C* **2019**, *123* (36), 22634–22642.

- (30) Müller, C. On the Glass Transition of Polymer Semiconductors and Its Impact on Polymer Solar Cell Stability. *Chem. Mater.* **2015**, *27* (8), 2740–2754.
- (31) Cheng, P.; Zhan, X. Stability of Organic Solar Cells: Challenges and Strategies. *Chem. Soc. Rev.* **2016**, *45* (9), 2544–2582.
- (32) Zhao, J.; Swinnen, A.; Van Assche, G.; Manca, J.; Vanderzande, D.; Mele, B. Van. Phase Diagram of P3HT/PCBM Blends and Its Implication for the Stability of Morphology. *J. Phys. Chem. B* **2009**, *113* (6), 1587–1591.
- (33) Heckler, I.; Kesters, J.; Defour, M.; Madsen, M.; Penxten, H.; D’Haen, J.; Van Mele, B.; Maes, W.; Bundgaard, E. The Influence of Conjugated Polymer Side Chain Manipulation on the Efficiency and Stability of Polymer Solar Cells. *Materials (Basel)*. **2016**, *9* (3), 181.
- (34) Brebels, J.; Kesters, J.; Defour, M.; Pirotte, G.; Van Mele, B.; Manca, J.; Lutsen, L.; Vanderzande, D.; Maes, W. A PCPDTTPD-Based Narrow Bandgap Conjugated Polyelectrolyte for Organic Solar Cells. *Polymer* **2018**, *137*, 303–311.
- (35) Demir, F.; Van den Brande, N.; Van Mele, B.; Bertho, S.; Vanderzande, D.; Manca, J.; Van Assche, G. Isothermal Crystallization of P3HT:PCBM Blends Studied by RHC. *J. Therm. Anal. Calorim.* **2011**, *105* (3), 845–849.
- (36) Defour, M.; Van den Brande, N.; Van Lokeren, L.; Van Assche, G.; Maes, W.; Vanderzande, D.; Van Mele, B. Influence of the Amorphous Phase and Preceding Solution Processing on the Eutectic Behaviour in the State Diagram of P3HT:PC61BM Determined by Rapid Heat–Cool Calorimetry. *RSC Adv.* **2016**, *6* (95), 92981–92988.
- (37) Mens, R.; Adriaenssens, P.; Lutsen, L.; Swinnen, A.; Bertho, S.; Ruttens, B.; D’Haen, J.; Manca, J.; Cleij, T.; Vanderzande, D.; Gelan, J. NMR Study of the Nanomorphology in Thin Films of Polymer Blends Used in Organic PV Devices: MDMO-PPV/PCBM. *J. Polym. Sci. Part A Polym. Chem.* **2008**, *46* (1), 138–145.
- (38) Piersimoni, F.; Chambon, S.; Vandewal, K.; Mens, R.; Boonen, T.; Gadisa, A.; Izquierdo, M.; Filippone, S.; Ruttens, B.; D’Haen, J.; *et al.* Influence of Fullerene Ordering on the Energy of the Charge-Transfer State and Open-Circuit Voltage in Polymer:Fullerene Solar Cells. *J. Phys. Chem. C* **2011**, *115* (21), 10873–10880.

- (39) Chambon, S.; Mens, R.; Vandewal, K.; Clodic, E.; Scharber, M.; Lutsen, L.; Gelan, J.; Manca, J.; Vanderzande, D.; Adriaenssens, P. Influence of Octanedithiol on the Nanomorphology of PCPDTBT:PCBM Blends Studied by Solid-State NMR. *Sol. Energy Mater. Sol. Cells* **2012**, *96*, 210–217.
- (40) Devisscher, D.; Reekmans, G.; Kesters, J.; Verstappen, P.; Benduhn, J.; Van den Brande, N.; Lutsen, L.; Manca, J.; Vanderzande, D.; Vandewal, K.; *et al.* Analysis of Bulk Heterojunction Organic Solar Cell Blends by Solid-State NMR Relaxometry and Sensitive External Quantum Efficiency – Impact of Polymer Side Chain Variation on Nanoscale Morphology. *Org. Electron.* **2019**, *74*, 309–314.
- (41) Danley, R. L.; Caulfield, P. A.; Aubuchon, S. R. A Rapid-Scanning Differential Scanning Calorimeter. *Am. Lab.* **2008**, *41* (1), 9–11.
- (42) Wouters, S.; Demir, F.; Beenaerts, L.; Van Assche, G. Calibration and Performance of a Fast-Scanning DSC—Project RHC. *Thermochim. Acta* **2012**, *530*, 64–72.
- (43) Van den Brande, N.; Van Assche, G.; Van Mele, B. Isothermal Structure Development in Submicron P3HT Layers Studied by Fast Scanning Chip Calorimetry. *Polymer* **2015**, *57*, 39–44.
- (44) Van den Brande, N.; Van Assche, G.; Van Mele, B. Isothermal Crystallization of PC61BM in Thin Layers Far below the Glass Transition Temperature. *Cryst. Growth Des.* **2015**, *15* (11), 5614–5623.
- (45) Van den Brande, N.; Van Assche, G.; Van Mele, B. Thermal Behaviour below and inside the Glass Transition Region of a Submicron P3HT Layer Studied by Fast Scanning Chip Calorimetry. *Polymer* **2016**, *83*, 59–66.
- (46) Van den Brande, N.; Van Assche, G.; Van Mele, B. Fast Scanning Chip Calorimetry Study of P3HT/PC61BM Submicron Layers: Structure Formation and Eutectic Behaviour. *Polym. Int.* **2019**, *68* (2), 277–282.
- (47) Gordon, M.; Taylor, J. S. Ideal Copolymers and the Second-Order Transitions of Synthetic Rubbers. i. Non-Crystalline Copolymers. *J. Appl. Chem.* **1952**, *2* (9), 493–500.
- (48) Welch, G. C.; Perez, L. A.; Hoven, C. V.; Zhang, Y.; Dang, X.-D.; Sharenko, A.;

- Toney, M. F.; Kramer, E. J.; Nguyen, T.-Q.; Bazan, G. C. A Modular Molecular Framework for Utility in Small-Molecule Solution-Processed Organic Photovoltaic Devices. *J. Mater. Chem.* **2011**, *21* (34), 12700.
- (49) Tang, A.; Li, L.; Lu, Z.; Huang, J.; Jia, H.; Zhan, C.; Tan, Z.; Li, Y.; Yao, J. Significant Improvement of Photovoltaic Performance by Embedding Thiophene in Solution-Processed Star-Shaped TPA-DPP Backbone. *J. Mater. Chem. A* **2013**, *1* (18), 5747.
- (50) Lequieu, W.; Van De Velde, P.; Du Prez, F. E.; Adriaenssens, P.; Storme, L.; Gelan, J. Solid State NMR Study of Segmented Polymer Networks: Fine-Tuning of Phase Morphology via Their Molecular Design. *Polymer* **2004**, *45* (23), 7943–7951.
- (51) Schmidt-Rohr, K.; Spiess, H. K. *Multidimensional Solid-State NMR and Polymers*; Elsevier, 1994; Vol. 100.
- (52) Clauss, J.; Schmidt-Rohr, K.; Spiess, H. W. Determination of Domain Sizes in Heterogeneous Polymers by Solid-state NMR. *Acta Polym.* **1993**, *44* (1), 1–17.
- (53) Wang, J.; Cheung, M. K.; Mi, Y. Miscibility in Blends of Poly (4-Vinylpyridine)/Poly (4-Vinylphenol) as Studied by ^{13}C Solid-State NMR. *Polymer* **2001**, *42* (7), 3087–3093.

TOC Graphic

